

# Stationary Spatial Patterns during Bulk CO Electrooxidation on Platinum

Antoine Bonnefont, Hamilton Varela, and Katharina Krischer\*

Fritz-Haber-Institut der MPG, Faradayweg 4-6, D-14195 Berlin, Germany, and Technische Universität München, Physik Department E19, James Franck Strasse 1, D-85748 Garching, Germany

Received: September 15, 2004; In Final Form: November 12, 2004

We present experimental studies and mathematical modeling on pattern formation during bulk CO electrooxidation on Pt ring electrodes. Profiles of the interfacial potential drop in front of the working electrode were recorded with a potential probe. Stationary self-organized potential patterns were observed under potentiostatic conditions in dilute acidic and basic supporting electrolytes. The amplitude and shape of these potential patterns can be modified by an appropriate local perturbation of the interfacial potential drop. A mathematical model of the formation of these patterns reveals that the homogeneous state becomes unstable through a subcritical Turing-like bifurcation and that several patterned electrode states coexist in wide parameter ranges.

## 1. Introduction

Carbon monoxide (CO) is usually considered to be a relatively simple molecule, suitable for basic studies on molecular adsorption and electrooxidation at the metal–electrolyte interface.<sup>1–19</sup> On platinum electrodes, CO oxidation is believed to take place through a Langmuir–Hinshelwood surface reaction in which adsorbed CO reacts with an adsorbed oxygen-containing species to form carbon dioxide, CO<sub>2</sub>, which readily leaves the surface.<sup>20</sup> In the case of bulk CO electrooxidation with controlled CO mass transport from the bulk of the electrolyte to the electrode surface, the experimental voltammetry exhibits a region of bistability which is, as theoretically shown, related to an S-shaped steady-state current–potential curve.<sup>21</sup> The middle branch of the S-shaped curve has a negative differential resistance (NDR) and is unstable under potentiostatic conditions, whereas the upper and lower branches are stable. An S-shaped current–potential curve implies that the system has the ability to spontaneously form nonequilibrium spatial patterns on the electrode surface.<sup>22,23</sup> In a previous paper,<sup>24</sup> we presented experimental studies and simulations on pattern formation during bulk CO electrooxidation on a rotating Pt-ring electrode in a low-conductivity electrolyte. If the electrolyte resistance is high enough, the S-shaped current–potential curve unfolds due to the ohmic potential drop through the electrolyte and it becomes possible to access a state on the NDR branch by potentiostatic means. Profiles of the electrode potential along the Pt-ring electrode were recorded with a potential probe. Two types of stationary, self-organized reaction patterns were observed in different ranges of the applied voltage. The first type of pattern with low amplitude appears on a steeply increasing branch of the current–voltage curve and could be qualitatively explained by a simple model where the fast spreading potential has an inhibitory effect on the autocatalytic reaction. The corresponding instability was shown to be a Turing-type bifurcation. Large amplitude structures with a considerably lower mean current density were observed at higher values of the applied voltage and are related to more complex chemical reactions.

This work was undertaken to complete our study of the properties of the low-amplitude patterns obtained during CO electrooxidation on a Pt ring electrode. We first present the evolution of the profile and the amplitude of the experimental patterns as a function of the applied outer voltage and the pH of the supporting electrolyte. The comparison of the experimental patterns with the numerical simulations of the formation of these patterns, using the spatially extended version of a basic homogeneous model for CO electrooxidation,<sup>21</sup> leads to a deeper understanding of the mechanisms that cause the observed spontaneous spatial symmetry breaking. In particular, the simulations confirmed experimental hints that stationary patterns with different amplitudes and wavelengths can coexist for the same values of the external parameters. The results are not only of fundamental importance but may also be applicable in the area of fuel cell technology since an intrinsically nonuniform reaction rate does not allow for complete poisoning of a Pt-based electrode with CO. Operating the cell in a nonhomogeneous state might thus improve considerably the CO tolerance and hence consequently the performance of the anode under dynamic conditions.

## 2. Experimental Section

The experimental setup is shown in Figure 1. A polycrystalline Pt ring embedded in cylindrical Teflon pieces was used as the working electrode (WE). The WE could be rotated around its axis at different rates. The Pt ring had a width of 1 mm and a mean circumference of 85 mm, the width being much smaller than the circumference and much smaller than the characteristic length of the patterns found (see below). Hence the electrode can be considered as “spatially one-dimensional”. The local electric potential in the electrolyte close to the WE along the angular direction,  $\theta$ , was measured versus the potential of the WE by means of a stationary potential probe (PP). The latter consisted of a J-shaped glass capillary whose tip was located approximately 1 mm from the WE and which was equipped with a Ag/AgCl electrode. During the rotation of the WE, the measurement of the voltage between the PP and the WE provided the distribution of the local interfacial potential drop,  $U_{pp}(\theta)$  in front of the Pt ring. Due to the potentiostatic control

\* Corresponding author. Email: krischer@ph.tum.de.

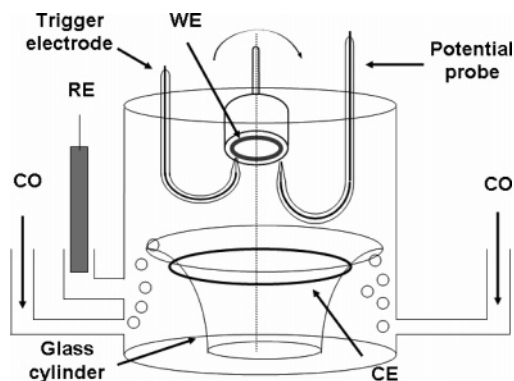


**Figure 1.** Scheme of the electrochemical cell. WE, working electrode; CE, counter electrode; RE, reference electrode.

employed,  $U_{pp}$  also contains information about the local current density. In addition, the rotation of the ring ensured a defined mass transport of CO from the bulk electrolyte to the WE.

To locally perturb the potential drop across the double layer of the WE, a trigger electrode was used which consisted of a Pt wire embedded in a J-shaped glass tube placed approximately 1 mm from the WE. The perturbation was achieved by applying 5 V between the trigger electrode and the WE for 25 ms by means of a function generator (Hameg, HM 8130).

Before each experiment, the Pt ring was polished to a mirror-like shine with diamond paste, down to 0.25  $\mu\text{m}$ , and washed thoroughly in acetone, ethanol, and then in Millipore water in an ultrasonic bath. To ensure radial symmetry in the electrochemical cell, the Pt counter electrode (CE) was also ring-shaped. It was located 40 mm from the WE. A saturated Hg/Hg<sub>2</sub>SO<sub>4</sub> electrode served as the reference electrode (RE). All experimental voltages are given with respect to this electrode. To avoid the presence of negative global feedback, which is induced through the potentiostat whenever the RE is close to the WE,<sup>25,26</sup> the RE was located below the plane of the CE. The voltage between the WE and the RE was controlled with a home-built potentiostat (FHI, E-lab). The electrolytic solution was prepared using Millipore water and HClO<sub>4</sub> (concentrated, Merck Suprapur) or KOH (Merck, pro analysis). Before each experiment, O<sub>2</sub> was removed from the electrolyte by bubbling N<sub>2</sub> (Linde, 5 N) through the electrochemical cell for 60 min. After the quality of the electrode had been checked by cyclic voltammetry, N<sub>2</sub> bubbling was replaced by CO bubbling (Air Liquide, 5 N) which was maintained during the entire experiment in order to keep the electrolyte saturated with CO.

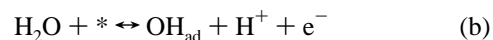
### 3. Spatially Extended Model for CO Bulk Electrooxidation

Our approach is based on a model introduced in ref 27 and further corroborated in ref 21 which reveals that CO electrooxidation possesses an S-shaped current–potential curve. The model takes into account three reaction steps that are consistent with a Langmuir–Hinshelwood reaction mechanism for CO electrooxidation on Pt. First, CO molecules adsorb on free adsorption sites of the Pt electrode surface, denoted by \*



Here, the subscripts s and ad indicate species in the reaction plane, i.e., just outside the double layer of the WE and species adsorbed on the electrode surface, respectively. The kinetics of CO adsorption is supposed to be independent of the double layer potential,  $\phi_{\text{dl}}$ . If the value of  $\phi_{\text{dl}}$  is high enough and free Pt sites are available, water is reversibly oxidized to platinum

hydroxide, PtOH



Adsorbed CO and OH can react to yield carbon dioxide which desorbs from the surface, thereby regenerating free platinum sites



This simple model does not include the irreversible formation of other platinum oxides, such as PtO or PtO<sub>2</sub>, that occurs at higher potential or the place exchange reactions of adsorbed oxygen species.<sup>28</sup> The transport of CO from the bulk of the solution to the surface of the electrode is accomplished by diffusion through a diffusion layer whose thickness depends on forced convective transport in the bulk electrolyte. The diffusive transport rate of CO between the bulk of the solution and the reaction plane can be symbolically written as



where the subscript b denotes a species in the bulk solution. The local rates corresponding to the adsorption of CO,  $\nu_{\text{CO,ads}}$ , adsorption and desorption of oxygen,  $\nu_{\text{OH,ads}}$  and  $\nu_{\text{OH,des}}$ , respectively, and the reaction between OH<sub>ad</sub> and CO<sub>ad</sub>,  $\nu_{\text{reac}}$ , were modeled by equations 1–4

$$\nu_{\text{CO,ads}} = k_{\text{CO,ads}} c_s (0.99 - \theta_{\text{CO}} - \theta_{\text{OH}}) \quad (1)$$

$$\nu_{\text{OH,ads}} = k_{\text{OH,ads}} \exp\left(\frac{\alpha F \phi_{\text{dl}}}{RT}\right) (\theta_{\text{OH}}^m (1 - \theta_{\text{CO}}) - \theta_{\text{OH}}) \quad (2)$$

$$\nu_{\text{reac}} = k_{\text{reac}} \exp\left(\frac{\alpha F \phi_{\text{dl}}}{RT}\right) \theta_{\text{OH}} \theta_{\text{CO}} \quad (3)$$

$$\nu_{\text{OH,des}} = k_{\text{OH,des}} \exp\left(\frac{-(1 - \alpha) F \phi_{\text{dl}}}{RT}\right) \theta_{\text{OH}} \quad (4)$$

$\theta_{\text{OH}}$  and  $\theta_{\text{CO}}$  are the coverages of OH<sub>ad</sub> and CO<sub>ad</sub>, respectively, and  $c_s$  is the concentration of CO in the reaction plane in front of the working electrode. For each charge-transfer reaction (b and c), a Butler–Volmer equation was used.  $R$  is the gas constant,  $T$  the absolute temperature, and  $\alpha$  the symmetry factor of reactions b and c. A maximum coverage of OH<sub>ad</sub>,  $\theta_{\text{OH}}^m$ , was assumed to avoid a complete blocking of CO adsorption by OH<sub>ad</sub> at high potential. For the rate of CO adsorption on the Pt surface, we assumed a maximum CO<sub>ad</sub> coverage of 0.99 in order to avoid a complete blocking of all reaction sites by CO. A maximum coverage of 1 would yield a steady state  $\theta_{\text{CO}} = 1$  and  $\theta_{\text{OH}} = 0$ , independent of the applied voltage, which is not physical. Note that the value of the bulk concentration of H<sup>+</sup> is included in the value of  $k_{\text{OH,des}}$ .

The spatially extended ring WE is described as a one-dimensional domain with periodic boundary conditions. The electrolyte is modeled as a cylindrical surface bounded at the top by the WE and at the bottom by the CE. Instead of assuming any specific kinetics at the counter electrode, we set the potential at the bottom of the cylinder to a constant value over the entire domain. The latter situation mimics a fast reaction at the counter electrode and assumes implicitly that the spatial potential variations behind the CE can be neglected. Furthermore, it is assumed that the bulk electrolyte is electroneutral and that the electrical conductivity in the electrolyte is uniform; then the distribution of the electrical potential  $\phi(x,z)$  within the bulk

electrolyte obeys Laplace's equation in an excellent approximation

$$\Delta\phi(x,z) = 0 \quad (5)$$

where  $x$  is the coordinate parallel to the WE and  $z$  is the direction perpendicular to the WE. The cylindrical geometry implies periodic boundary conditions in the  $x$ -coordinate,  $\phi(x,z,t) = \phi(x + L, z, t)$ ,  $L$  being the length (circumference) of the WE. At the bottom of the cylinder ( $z = 0$ ) along the counter electrode, the potential is set to zero,  $\phi(x, z = 0) = 0$ , and the potentiostatic operation mode is described by the following constraint:

$$U = \phi_{\text{dl}}(x) + \phi(x, z = -w) \quad (6)$$

where  $U$  is the outer voltage and  $\phi_{\text{dl}}(x)$  the potential drop across the double layer of the WE. At the working electrode, i.e., at  $z = -w$ , the evolution of the interfacial potential,  $\phi_{\text{dl}}$ , follows from the charge balance at a given location on the working electrode

$$C_o \frac{\partial \phi_{\text{dl}}(x)}{\partial t} = -i_F(x) - \sigma \frac{\partial \phi(x, z)}{\partial z} \Big|_{z=-w} \quad (7)$$

where  $C_o$  is the specific capacitance of the double layer and  $\sigma$  the conductivity of the electrolyte. The local Faradaic current density at the working electrode is represented by  $i_F(x)$ ; according to reactions a–c it is given by

$$i_F(x) = FS_{\text{tot}}[\nu_{\text{OH,ads}}(x) + \nu_{\text{reac}}(x) - \nu_{\text{OH,des}}(x)] \quad (8)$$

$F$  is the Faraday constant and  $S_{\text{tot}}$  the concentration of surface sites. The temporal evolutions of the coverages,  $\theta_{\text{OH}}$ ,  $\theta_{\text{CO}}$ , and of  $c_s$  are described by the following set of partial differential equations:

$$\frac{\partial \theta_{\text{CO}}(x)}{\partial t} = \nu_{\text{CO,ads}} - \nu_{\text{reac}} \quad (9)$$

$$\frac{\partial \theta_{\text{OH}}(x)}{\partial t} = \nu_{\text{OH,ads}} - \nu_{\text{reac}} - \nu_{\text{OH,des}} \quad (10)$$

$$\frac{\partial c_s(x)}{\partial t} = -\frac{2S_{\text{tot}}}{\delta} \nu_{\text{CO,ads}} + \frac{2D_1}{\delta^2} (c_b - c_s) + D_2 \frac{\partial^2 c_s}{\partial x^2} \quad (11)$$

For the transport of CO from the bulk of the solution to the surface of the electrode (second term of the right hand side of eq 11), we assumed a linear concentration gradient across a diffusion layer of thickness  $\delta$ . The CO concentration in the bulk of the electrolyte is represented by  $c_b$ . The surface diffusion of  $\text{CO}_{\text{ad}}$  and  $\text{OH}_{\text{ad}}$  is neglected since it is small compared to the lateral diffusion of  $\text{CO}_s$ .

With the simple cylindrical geometry, Laplace's eq 5 can be solved analytically,<sup>22,29</sup> the solution being a Fourier series in the  $x$ -direction. We used this solution to project equations 9–11 and 7 on the Fourier basis functions, the numerical integration being performed by a pseudospectral method. Table 1 shows the values of the numerical parameters used in the simulations. The values of most parameters are taken from the homogeneous model published in ref 21. There it was shown that these parameters reproduce well the experimentally measured cyclic voltammograms and that the correct dependences of the cyclic voltammograms on external parameters, such as the rotation rate of the electrode or the sweep rate, are obtained. Note, however, that only a few of these parameters were experimentally determined. We verified that a smooth change in any of

**TABLE 1: Numerical Values of the Parameters Used for the Simulations**

parameter (unit)	value	parameter (unit)	value
$L$ (cm)	1	$C_o$ (F cm <sup>-2</sup> )	$2 \times 10^{-5}$
$c_b$ (mol L <sup>-1</sup> )	$10^{-3}$	$w$ (cm)	4.0
$D_1$ (cm <sup>2</sup> s <sup>-1</sup> )	$5 \times 10^{-5}$	$k_{\text{OH,ads}}$ (s <sup>-1</sup> )	$10^{-4}$
$D_2$ (cm <sup>2</sup> s <sup>-1</sup> )	$5 \times 10^{-3}$	$k_{\text{OH,des}}$ (s <sup>-1</sup> )	$10^5$
$\delta$ (cm)	0.0067, 0.0027	$k_{\text{CO,ads}}$ (cm <sup>3</sup> mol <sup>-1</sup> s <sup>-1</sup> )	$10^8$
$S_{\text{tot}}$ (mol cm <sup>-2</sup> )	$2.2 \times 10^{-9}$	$k_r$ (s <sup>-1</sup> )	$10^{-5}$
$\sigma$ (Ωcm)	$2 \times 10^{-2}$	$\theta_{\text{OH}}^m$	0.333

these parameters does not qualitatively alter the dynamics, while a large change in certain parameters often requires changes in other parameters to retain the S-shaped current–potential curve. Sixty-four Fourier modes were used for numerical integrations. With the parameters given in Table 1, the number of unstable modes is smaller than 15. Note that the diffusion coefficient parallel to the working electrode,  $D_2$ , was made to be 100 times larger than the diffusion coefficient perpendicular to the electrode. A slightly larger value of  $D_2$  compared to  $D_1$  is realistic in order to qualitatively account for the radial diffusion at the ring electrode. The much larger value was chosen for computational reasons since it reduces the number of unstable modes in the calculation considerably without significantly changing the position of the maximum of the dispersion curve. Hence, the calculations can be done with fewer modes, and the calculation time is drastically reduced.

#### 4. Results

A typical current–voltage curve of Pt in CO-saturated diluted (2 mM) perchloric acid and the corresponding stationary potential pattern formation observed when fixing the outer voltage,  $U$ , somewhere in the voltage range in which the current increased linearly were published previously.<sup>24</sup> Similar potential patterns were obtained in the case of CO electrooxidation in a diluted (2 mM) basic electrolyte as shown in Figure 2. In the lower graph of Figure 2, the applied voltage,  $U$  (blue curve), and the corresponding current response (red curve) are shown as a function of time. The upper part of Figure 2 displays the inhomogeneous part of the PP signal as a function of the angular coordinate  $\theta$  (i.e., along the ring electrode) and time. The inhomogeneous part of the PP signal was obtained by subtracting at each instant in time the spatial average,  $\langle U_{\text{pp}} \rangle(t)$ , from  $U_{\text{pp}}(\theta, t)$ . Since the homogeneous part of the probe signal varies with the applied voltage, subtraction of the spatial average allows a better view of the inhomogeneous part of the potential probe

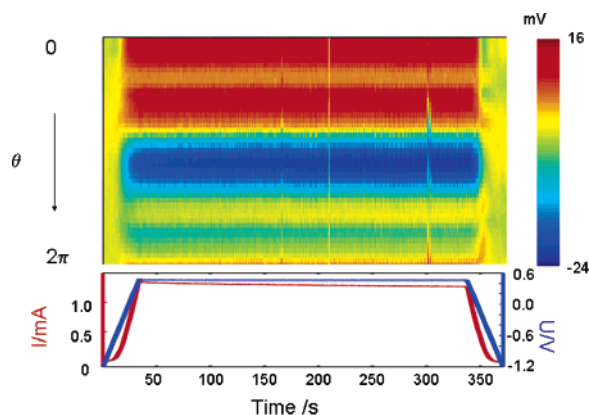


**Figure 2.** Top: Position–time plot of the inhomogeneous part of the potential probe signal during bulk CO electrooxidation in 2 mM KOH. Bottom: Corresponding applied voltage (blue line) and total current (red line) vs time. Rotation speed of the electrode  $\omega = 1200$  rpm.



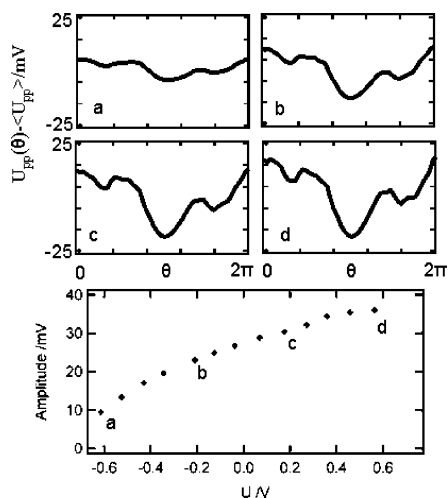


**Figure 3.** Top: Potential profiles recorded during stationary bulk CO electrooxidation in 2 mM KOH. (a)  $U = -0.6$  V. (b)  $U = -0.2$  V. (c)  $U = 0.2$  V. (d)  $U = 0.6$  V. Bottom: Peak to peak amplitude of the profiles for different values of the outer applied voltage  $U$ . Rotation speed of the electrode  $\omega = 1200$  rpm.

signal. Figure 2 shows that during a positive voltage sweep that starts at  $-1.2$  V, a potential pattern emerges on the Pt ring working electrode at  $U \approx -0.6$  V. When the external voltage is held at  $U = 0.5$  V, i.e., within the linear current increase regime, the potential pattern remains stationary, its amplitude (peak to peak) being approximately 40 mV. These stationary potential structures disappear during the reverse scan of the outer voltage.

Stationary potential profiles for different values of the outer applied voltage,  $U$ , are displayed in the upper part of Figure 3. Each potential profile was obtained in the following way:  $U$  was scanned with a sweep rate of  $100 \text{ mV s}^{-1}$  from  $-1.2$  V to more positive values until the desired value of  $U$  was reached and then kept constant for 5 min before the profile was recorded. The relaxation of the potential profiles to a stationary state occurred in less than 5 min, ensuring that the transients had decayed before the patterns were recorded. Fourier analysis of the shapes of the potential patterns (not shown) revealed that the profiles are dominated by Fourier modes with wavenumbers  $n = 1, 2$ , and  $3$ . In the lower part of Figure 3, the peak to peak amplitude of different potential profiles is plotted vs  $U$ . The peak to peak amplitude of the stationary potential pattern monotonically increases with  $U$ , the increase becoming small for  $U > 0.4$  V suggesting that the amplitude saturates at a value close to 40 mV at high  $U$ . However, it was not possible to experimentally confirm the saturation of the amplitude because when the applied voltage,  $U$ , was increased further, the global current drastically decreased and another type of potential pattern emerged, as reported previously.<sup>24</sup>

For the sake of comparison, the upper part of Figure 4 shows the profiles  $U_{pp}(\theta) - \langle U_{pp} \rangle$  of the stationary potential pattern obtained in a 2 mM  $\text{HClO}_4$  electrolyte solution for different values of  $U$ . On the lower part of Figure 4, the peak to peak amplitudes of these profiles obtained in a weakly acidic solution are displayed as a function of the applied voltage. Each potential profile plotted in Figure 4 was obtained in a manner similar to that of the profiles plotted in Figure 3:  $U$  was scanned with a sweep rate of  $50 \text{ mV s}^{-1}$  from  $-0.2$  V to more positive values and kept constant for some time after the desired value of  $U$  had been reached; a stationary potential pattern adjusted quickly on the working electrode and was recorded after approximately 2 min when all of the transients had died out. For experiments

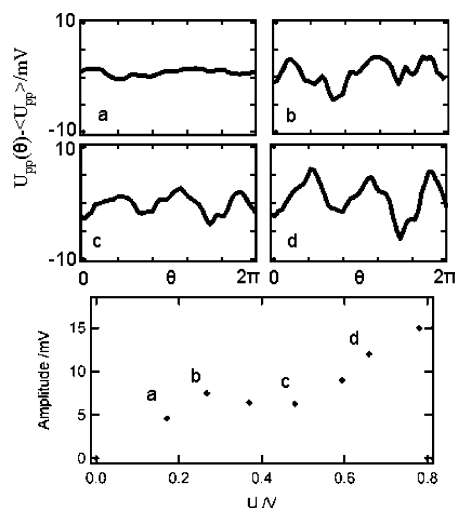


**Figure 4.** Top: Potential profiles recorded during stationary bulk CO electrooxidation in 2 mM  $\text{HClO}_4$ . (a)  $U = 0.17$  V. (b)  $U = 0.27$  V. (c)  $U = 0.48$  V. (d)  $U = 0.66$  V. Bottom: Peak to peak amplitude of the potential profiles for different values of the outer applied voltage  $U$ . Rotation speed of the electrode  $\omega = 1200$  rpm.

in acidic solution, the applied voltage range was restricted to  $-0.2 \text{ V} < U < 0.7 \text{ V}$ . As in the case of the experiment in a basic supporting electrolyte, the upper limit is due to the transition to large amplitude structures which occurred for  $U > 0.7$  V. As some spatiotemporal potential patterns were observed at the working electrode during the CO oxidation pre-peak,<sup>30</sup> the lower limit of the outer voltage range was chosen so that no interference with the CO oxidation pre-peak<sup>31–33</sup> occurred.

A comparison of Figures 3 and 4 shows that low-amplitude structures exist in a narrower applied voltage range in the case of the acidic solution than in the basic one for approximately the same electrolyte resistance. In alkaline solution, the  $U$ -window in which patterns form is about 1200 mV, while in acidic solution, it is only 600 mV wide. Furthermore, in acidic solution the shape of the potential pattern changed qualitatively when the outer voltage,  $U$ , increased (cf. Figure 4), the amplitude did not monotonically increase with  $U$ , and its maximum amplitude was only half that of the one in alkaline solution.

The response of the electrochemical system to a local perturbation of the potential profile of the spatiotemporal patterns was investigated experimentally by applying local potential pulses between a small trigger electrode and the working electrode. Two examples of such measurements in a basic electrolyte are shown in Figure 5. In both cases, the perturbation was applied for 25 ms after a stationary potential pattern was established, and the rotation frequency of the WE was 10 Hz. Thus, one rotation of the working electrode lasted 100 ms and the potential perturbation was localized on one-fourth of the ring electrode. The example in Figure 5a represents the more typical response. Here, the pulse caused a change in the amplitude of the stationary potential pattern to larger values (from ca. 30 to ca. 60 mV) without significant change in the pattern shape or its location on the Pt ring. Interestingly, the change in amplitude of the pattern occurred without a change in the global current (except for a short current peak concomitant with the application of the voltage pulse) indicating that the local increase of the reaction rate in some regions of the electrode is approximately compensated by a decrease of the reaction rate in the other regions. Note that the potential pattern with higher amplitude resulting from the potential pulse remains when the voltage scan starts again, even during the back scan.

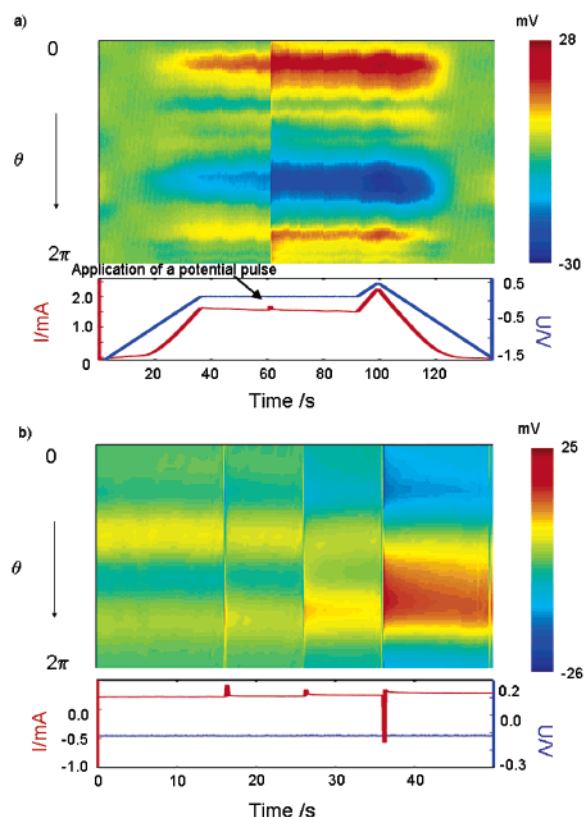


**Figure 5.** Position–time plots of the inhomogeneous part of the potential probe signal during bulk CO electrooxidation in 3 mM KOH demonstrating the effect of a trigger pulse on the potential pattern and corresponding applied voltage (blue line) and total current (red line) vs time. Rotation speed of the electrode  $\omega = 600$  rpm. (a) The trigger pulse (at  $t \approx 60$  s) leads to a change in the amplitude of the pattern but not in its shape. (b) The application of three pulses causes a transition between patterns with both different amplitudes and shapes.

Figure 5b shows an example which demonstrates that a voltage pulse might alter not only the amplitude of the pattern but also its shape. Here, three pulses were applied, each one manifesting itself as a spike in the global current. After the first pulse, the system relaxed back to the original pattern which was dominated by a Fourier mode with a wavenumber of 3. The second and third pulses, both, caused significant changes in the shape of the pattern, the final pattern having a wavenumber of one and a considerably larger amplitude.

Let us now turn to our theoretical investigations on the dependence of the amplitudes and shapes of the patterns on the applied voltage. The simulations were carried out using the spatially extended model described in section 3. The upper part of Figure 6a shows the inhomogeneous part of the calculated spatial potential distribution,  $\phi_{\text{dl}}(\theta) - \langle \phi_{\text{dl}} \rangle$ , and the lower part shows the applied voltage,  $U$ , and the total current,  $I$ , vs time. The potential profiles and the current–potential curve were obtained using the following procedure: for the  $n$ th value of the outer voltage  $U_n = U_0 + n\Delta U$ , the evolution of the potential distribution along the working electrode is computed during a time  $\Delta t$  which was long enough to reach stationary conditions and using the stationary solutions obtained at  $U = U_{n-1}$  as initial conditions.

Consider first the lower part of Figure 6a. Because of the low value of the electrolyte conductivity,  $\sigma$ , chosen, the shape of the current–voltage characteristic is strongly affected by the ohmic potential drop, as in the experiments. Consequently, on the positive and negative scans, there is a voltage region in which the current increases linearly with  $U$ .<sup>24</sup> When entering

and leaving this region, the current exhibits a small jump. A comparison with the upper part of Figure 6a reveals that the small jumps in total current occur when a pattern forms or disappears on the electrode. For the chosen parameter values, the pattern exhibits one maximum and one minimum, the difference between the two amounting to about 10 mV, similar to the experiments. Spatial profiles of the four variables  $\phi_{\text{dl}}(\theta)$ ,  $\theta_{\text{OH}}(\theta)$ ,  $\theta_{\text{CO}}(\theta)$ , and  $c_{\text{S}}(\theta)$  are displayed in Figure 6b for  $U = 0.975$  V. In the domain in which the interfacial potential  $\phi_{\text{dl}}$  at the electrode is higher, hydroxide coverage, and thus Faradaic current, is low whereas the CO coverage is close to its saturation value. Correspondingly, the hydroxide coverage is much higher at lower values of  $\phi_{\text{dl}}$  allowing a high reaction rate which keeps the CO coverage low. It is noteworthy that the amplitudes of the coverages of CO and OH are (nearly 1 and 0.333 ML, respectively) close to the possible maximum values while the potential profile exhibits only variations of about 10 mV. The counterintuitive phase shift of approximately  $180^\circ$  between the OH coverage on the electrode and the distribution of  $\phi_{\text{dl}}$  reflects the autocatalytic increase of the reaction current with hydroxide coverage on the negative differential resistance (NDR) branch of the S-shaped current– $\phi_{\text{dl}}$  curve.<sup>24</sup>

It is evident from Figure 6a that the calculated potential profiles depend on the voltage value, the size of the domain with a high value of  $\phi_{\text{dl}}$  decreasing with  $U$ . The plot of pattern amplitude versus  $U$  in Figure 7 was obtained from the data in Figure 6a by taking the peak to peak amplitude for different values of  $U$  during both voltage scans. The peak to peak amplitude increases monotonically with the voltage in the range of  $0.86 \text{ V} < U < 0.94 \text{ V}$ , reaches a maximum with  $U \approx 0.94$  V, and decreases with  $U > 0.94$  V.

Another remarkable feature of the patterned electrode state present in the calculated voltammogram displayed in Figure 6a is its hysteretic behavior. It emerged at  $U = 0.90$  V during the forward voltage scan and disappeared at  $U = 1.02$  V, whereas the potential pattern emerged at  $U = 0.99$  V and disappeared at  $U = 0.85$  V during the backward voltage scan. This means that there are two voltage ranges ( $0.85 \text{ V} < U < 0.90$  V and  $0.99 \text{ V} < U < 1.02$  V) in which the patterned electrode state and the homogeneous electrode state are both stable solutions of the set of equations. The hysteresis can be seen in Figure 8 where the stationary S-shaped  $I$ – $\phi_{\text{dl}}$  curve of the homogeneous state (obtained from a continuation of the homogeneous solution) and the  $I$ – $\langle \phi_{\text{dl}}(\theta) \rangle$  curve (obtained from the data of Figure 6) are displayed in blue and red, respectively. The dotted curve represents the unstable homogeneous state. During the forward voltage scan, the two current–potential curves coincide until the uniform state becomes unstable. The bifurcation point lies very close to the point at which the system enters the NDR branch of the  $I$ – $\phi_{\text{dl}}$  curve. However, during the backward voltage scan, the electrode patterned state remains stable beyond the  $U$  value at which the homogeneous state becomes unstable and for a voltage range of approximately 50 mV both states coexist. A corresponding though somewhat smaller hysteresis exists around the high current turning point of the current–voltage curve. Note that in the  $I$ – $\langle \phi_{\text{dl}}(\theta) \rangle$  curve corresponding to the patterned state, the negative differential resistance is much less pronounced than that of the (mainly unstable) homogeneous state, and thus, the dependence of  $I$  on  $\langle \phi_{\text{dl}}(\theta) \rangle$  is considerably enhanced.

When mass transport is more efficient, i.e., for smaller values of  $\delta$ , the behavior becomes even more complex. This can be seen in Figure 9. Here, in the same representation as in Figure 6a, the results of a simulation in which only the value of the

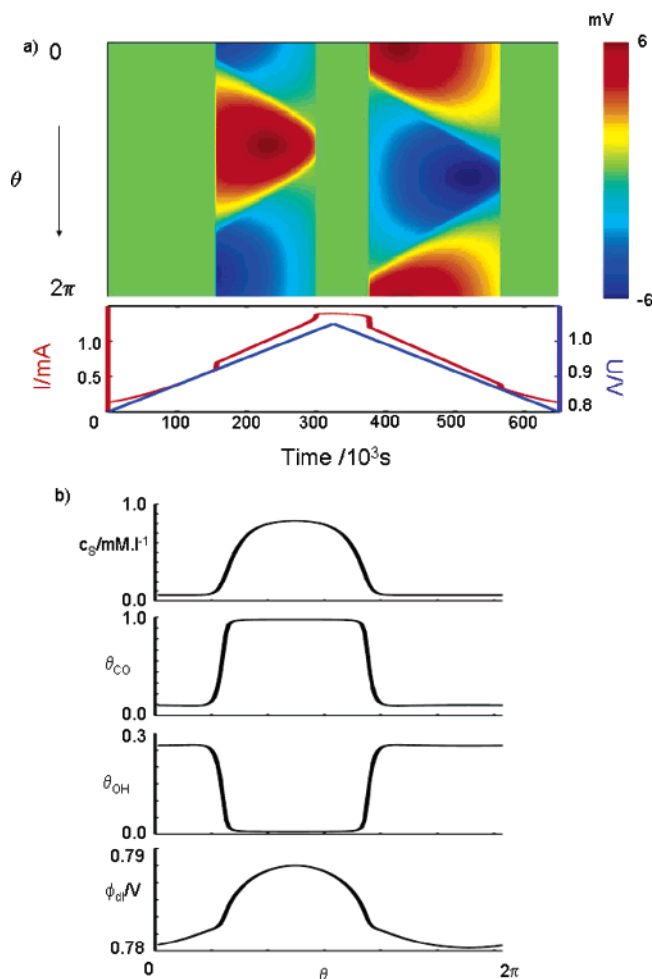


**Figure 6.** (a) Top: Position–time plot of the inhomogeneous part of the calculated stationary electrode potential,  $\phi_{dl}$ , during a cyclic change in  $U$ .  $\delta = 0.0067$  cm. See Table 1 for the remaining parameters. Bottom: Corresponding total current in red and of  $U$  in blue. (b) Calculated spatial distribution of the different variables  $\phi_{dl}(\theta)$ ,  $\theta_{OH}(\theta)$ ,  $\theta_{CO}(\theta)$ , and  $c(\theta)$  plotted for  $U = 0.975$  V.

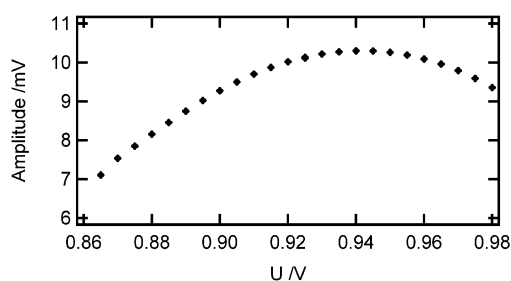


**Figure 7.** Peak to peak amplitude of the calculated potential patterns for different values of the outer voltage  $U$  for the same parameters as in Figure 6.

diffusion layer thickness  $\delta$  was lowered from that of the previous one are shown. During the positive scan, a pattern with three maxima and three minima with an amplitude of about 6.5 mV emerged from the homogeneous state at a critical value of  $U$ . When the outer voltage was increased, the shape of the pattern at first remained qualitatively the same, its amplitude increasing slightly to about 9 mV. Then, it was replaced by an asymmetric pattern with two maxima that in turn was followed by one with only one maximum, and finally by the homogeneous state. During the backward scan of the voltage, the uniform potential distribution on the working electrode gave way to a potential

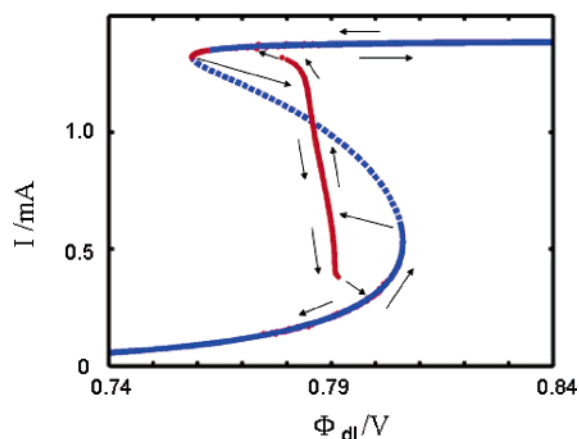


**Figure 8.** Calculated stationary current–potential curves for  $\delta = 67$   $\mu\text{m}$ . Blue curve:  $I$ – $\phi_{dl}$  of the homogeneous stationary state. Red curve:  $I$ – $\langle\phi_{dl}(\theta)\rangle$  for the patterned state of Figure 6. The arrows indicate the direction of voltage change. The dotted line indicates the unstable homogeneous state.

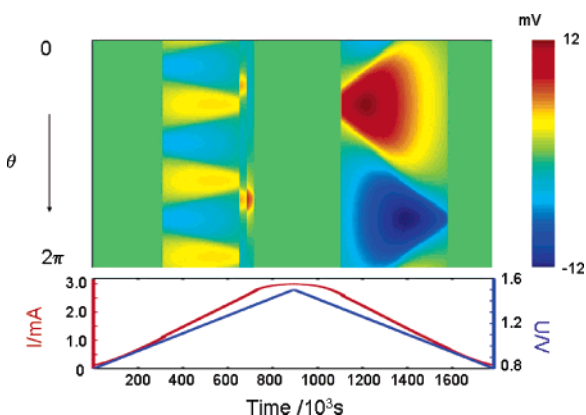


**Figure 9.** Top: Position–time plot of the inhomogeneous part of the calculated electrode potential,  $\phi_{dl}$ , during a cyclic change in  $U$ .  $\delta = 27$   $\mu\text{m}$ . See Table 1 for the remaining parameters. Bottom: Corresponding total current in red and of  $U$  in blue.

pattern with a wavenumber of 1 and a maximum amplitude of about 24 mV which was 3 times larger than the amplitude of the patterns obtained during the forward scan. Note that during the backward scan the global current had about the same values as in the forward scan. In contrast to the forward scan, the pattern existed in a wide voltage region and was the only pattern that was established during the back scan. Hence, different patterns with different amplitudes can coexist for the same parameters, and the selection of wavelength and amplitude of the patterns is very sensitive to the initial state of the electrode.

To further corroborate the existence and coexistence regions of the three different patterns of Figure 9, we carried out simulations in which the different patterned solutions of the forward scan were continued in both scan directions. In Figure 10a, the corresponding stationary current–voltage curves of the stationary homogeneous state (which was again obtained by continuation methods and thus also unstable homogeneous states were tracked) (blue curve) and of the wavenumber 1, 2, and 3 patterns (red, green, and black, respectively) are plotted. The blue dotted line indicates the voltage region in which a homogeneous stationary solution is unstable. Within most of this region, all three of the nontrivial solutions are linearly stable and thus coexist. Moreover, at the low-voltage end of the pattern region there is a small interval in which all three stationary patterns also coexist with the homogeneous state. The existence regions of the wavenumber 2 and 1 patterns extend at positive



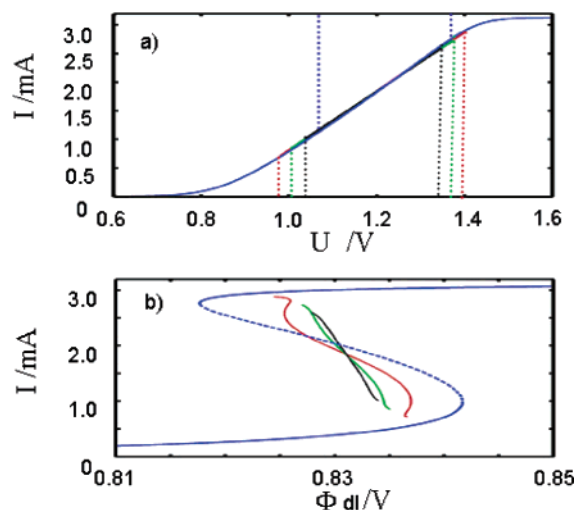


**Figure 10.** (a) Current–voltage plots corresponding to the different patterns shown in Figure 9. Blue, homogeneous state; black, wavenumber 3 pattern; green, wavenumber 2 pattern; red, wavenumber 1 pattern. The dashed lines indicate the existence regions of the respective solutions. (b) Stationary current–potential plots  $I-\langle\phi_{dl}(\theta)\rangle$  corresponding to the different patterns shown in Figure 9. Labeling as in (a).

voltages beyond the region in which the homogeneous state is unstable. While the  $I-U$  curves of the individual states lie practically on top of each other, they are well separated when plotting  $I$  vs the mean double layer potential. This can be seen in Figure 10b, where for each of the four patterns appearing in Figure 10a,  $I$  is plotted vs the mean double layer potential for all values of  $U$  in which the respective pattern exists (see dashed lines in Figure 10a). Two important observations can be made: First, in case of a patterned electrode state, the current–potential curves exhibit a different shape when compared to the homogeneous electrode S–NDR branch, the NDR being less pronounced, some parts of the  $I-\langle\phi_{dl}(\theta)\rangle$  curve, in red, even being without a negative differential resistance. Second, there is no smooth transition from the homogeneous state to a patterned state. Linear stability analysis revealed that the homogeneous state becomes unstable through a Turing-type bifurcation; i.e., the dispersion curve of the real part of the eigenvalue vs wavenumber exhibits a maximum and crosses zero at the bifurcation point. These two points suggest that the homogeneous state becomes unstable through a subcritical Turing bifurcation.

## 5. Discussion

In this work, we showed that stationary potential patterns spontaneously form on a platinum working electrode during bulk CO electrooxidation in a dilute acidic solution as well as in a dilute basic solution. Most aspects of the experimentally observed patterns were reproduced in a mathematical model allowing deeper insight into the cooperative phenomena occurring inevitably during CO electrooxidation in some parameter ranges.

Let us first compare the experimental results in weakly acidic and weakly basic electrolytes. Although the qualitative behavior is similar in both electrolytes, i.e., the electrode exhibits a spontaneous transition from the homogeneous state to a stationary pattern in the region of  $U$  in which the current–voltage curve possesses a linearly increasing branch, there are also differences. In a basic solution, the potential patterns keep the same shape and the peak to peak amplitude increases monotonically with  $U$ ; on the other hand, the potential pattern in

perchloric acid exhibits a change in shape at  $U \approx 0.4$  V, and the amplitude is larger than in acidic solution. Furthermore, the potential patterns exist in a wider voltage range in basic solution than in acidic solution for similar values of the supporting electrolyte resistance. Furthermore, in agreement with experiments reported by Schmidt et al.,<sup>14</sup> we observed a significant CO electrooxidation rate in the alkaline electrolyte even in a voltage range close to the hydrogen underpotential deposition region. The later onset of CO oxidation in an acidic solution was attributed to the inhibition of surface oxide formation because of the adsorption of anions from the supporting electrolyte.<sup>34,35</sup> Thus, anions compete with both CO in solution and water for free platinum sites shifting the onset of CO oxidation to more positive values. The larger existence range of the patterns points to the fact that even at values of  $\phi_{dl}$  close to the H-upd region the CO-oxidation rate is high enough to support the positive feedback loop present in reactions a–d. The voltage limit up to which the small amplitude patterns existed (vs RHE) was larger in alkaline than in acidic solutions for both negative and positive potentials. At positive potentials, the existence range is limited by the formation of large amplitude structures.<sup>24</sup> Hence, the formation of the latter is pH-dependent in a nontrivial way.

Next let us compare the experiments with the calculations. As already mentioned, the simulations qualitatively capture the main characteristics of the experiments, namely, the spontaneous emergence of stationary structures in diluted electrolytes on the unfolded S–NDR branch of the S-shaped  $I-\phi_{dl}$  curve of the homogeneous system. This strongly suggests that the experimentally observed stationary structures are indeed the result of the autocatalytic removal and buildup of the CO adlayer, and thus, they are the result of the Langmuir–Hinshelwood mechanism coupled to mass transport control in the reactive region and the inhibitory and long range effect of the electrode potential.

A more intricate result of the calculations is that several patterned states can coexist in a certain range of  $U$ . Experimentally, this was tested by perturbing the electrode potential locally, thereby triggering transitions from patterns with a small amplitude to those with a large amplitude. Sometimes, the change in amplitude went along with a change in the dominant wavenumber. More often, the change in amplitude was not accompanied by a significant change in shape. However, a transition of the latter type could not be found in the simulations. This discrepancy seems to be closely related to another important difference between the experimental and calculated patterns, namely that the profile of the calculated potential patterns changes continuously with the applied voltage, the domains with lower interfacial potential,  $\phi_{dl}$ , becoming wider as  $U$  increases, whereas the profile of the potential pattern in alkaline solution does not change over a broad range of  $U$ . The origin of both seems to be the sensitivity of the pattern shape to small inhomogeneities of the electrode surface caused by the pretreatment. In general, on a specific day, the same pattern profile was always observed even if some changes in the pattern shape can be observed in a diluted perchloric acid electrolyte when  $U$  increases (Figure 4). Furthermore, keeping the electrode for a few minutes in the patterned region at high potential left an imprint on the electrode that manifested itself locally in the different reaction rates in the hydrogen evolution region where the electrode potential was homogeneous before starting CO electrooxidation. This suggests that CO oxidation can modify the structure of the substrate, most likely by roughening the surface. Both facts make experimental investigation of the

patterns more difficult. Hence, the question of whether homogeneous and patterned states coexist in some  $U$  interval could not be unambiguously answered.

Nevertheless, other, even subtle, aspects compare favorably between the experiments and calculations. The rotation rate of the working electrode ensures a defined mass transport of CO to the electrode surface through the control of the diffusion layer thickness,  $\delta$ . The model of Koper et al.<sup>21</sup> predicts that the size of the bistable region in the current–potential curve increases when  $\delta$  increases or when the rotation rate of the electrode decreases. A comparison of Figures 6 and 9 shows that the number of excited modes, and thus the wavenumber of the pattern, tend to become smaller when the rotation rate of the electrode is reduced. Such a tendency could be observed experimentally, although, much care has to be taken to ensure that the patterns were not pinned to electrode defects. Another remarkable feature is that the amplitude of the current jump concomitant with the potential pattern emergence (cf. Figure 6) decreases when the rotation rate of the electrode increases (cf. Figure 9). This could explain why no current jump was experimentally observed even at a slow scanning rate of the outer voltage.

## 6. Conclusion

CO electrooxidation is one of the few electrochemical systems exhibiting an S-shaped current–potential curve. The observation of stationary self-organized patterns during CO oxidation is an important validation of the theoretical predictions on pattern formation in S–NDR systems. Above that, a study of pattern formation allows us to validate or identify the reaction steps that prevail under certain experimental conditions. The measurements reported here revealed that in a low-concentration alkaline supporting electrolyte the Langmuir–Hinshelwood mechanism seems operative even close to the H-up region. Furthermore, the results form a basis for further studies on pattern formation during CO electrooxidation in a parameter region where different positive feedback loops are present, as in the large amplitude structures reported.<sup>24</sup> Finally, the results pointed to a further complication that exists for bulk CO oxidation, namely, a reaction-induced change of the electrode surface morphology, an observation that certainly calls for further detailed studies.

**Acknowledgment.** A.B. thanks the European Commission for support by a Marie-Curie fellowship.

## References and Notes

- (1) Beden, B.; Bilmes, S.; Lamy, C.; Léger, J. M. *J. Electroanal. Chem.* **1983**, *149*, 295.
- (2) Clavilier, J.; Albalat, R.; Gomez, R.; Orts, J. M.; Feliu, J. M.; Aldaz, A. *J. Electroanal. Chem.* **1992**, *330*, 489.
- (3) Weaver, M. J.; Chang, S. C.; Leung, L. W.; Jiang, X.; Rubel, M.; Szklarczyk, M.; Zurawski, D.; Wieckowski, A. *J. Electroanal. Chem.* **1992**, *327*, 261.
- (4) Gasteiger, H. A.; Markovic, N.; Ross, P. N.; Cairns, E. J. *J. Phys. Chem.* **1994**, *98*, 617.
- (5) Villegas, I.; Weaver, M. J. *J. Chem. Phys.* **1994**, *110*, 1648.
- (6) Arico, A. S.; Modica, E.; Passalacqua, E.; Antonucci, V.; Antonucci, P. L. *J. Appl. Electrochem.* **1997**, *27*, 1275.
- (7) Petukhov, A. V.; Akemann, W.; Friedrich, K. A.; Stimming, U. *Surf. Sci.* **1998**, *402–404*, 182.
- (8) Markovic, N. M.; Grgur, B. N.; Lucas, C. A.; Ross, P. N. *J. Phys. Chem. B* **1999**, *103*, 487.
- (9) Lin, W. F.; Iwasita, T.; Vielstich, W. *J. Phys. Chem. B* **1999**, *103*, 3250.
- (10) Lin, W. F.; Zei, M. S.; Eiswirth, M.; Ertl, G.; Iwasita, T.; Vielstich, W. *J. Phys. Chem. B* **1999**, *103*, 6968.
- (11) Markovic, N. M.; Lucas, C. A.; Grgur, B. N.; Ross, P. N. *J. Phys. Chem. B* **1999**, *103*, 9616.
- (12) Couto, A.; Rincon, A.; Perez, M. C.; Gutiérrez, C. *Electrochim. Acta* **2001**, *46*, 1285.
- (13) Perez, M. C.; Rincon, A.; Gutiérrez, C. *J. Electroanal. Chem.* **2001**, *511*, 39.
- (14) Schmidt, T. J.; Ross, P. N.; Markovic, N. M. *J. Phys. Chem. B* **2001**, *105*, 12082.
- (15) Jusys, Z.; Kaiser, J.; Behm, R. J. *Phys. Chem. Chem. Phys.* **2001**, *3*, 4650.
- (16) Lebedeva, N. P.; Koper, M. T. M.; Feliu, J. M.; van Santem, R. A. *J. Electroanal. Chem.* **2002**, *524*, 242.
- (17) Lebedeva, N. P.; Koper, M. T. M.; Feliu, J. M.; van Santem, R. A. *J. Phys. Chem. B* **2002**, *106*, 12938.
- (18) Anderson, A. B.; Neshev, N. M. *J. Electrochem. Soc.* **2002**, *149*, E383.
- (19) Chou, K. C.; Markovic, N. M.; Kim, J.; Ross, P. N.; Somorjai, G. A. *J. Phys. Chem. B* **2003**, *107*, 1840.
- (20) Gilman, P. J. *J. Phys. Chem.* **1964**, *68*, 70.
- (21) Koper, M. T. M.; Schmidt, T. J.; Markovic, N. M.; Ross, P. N. *J. Phys. Chem. B* **2001**, *105*, 8381.
- (22) Mazouz, N.; Krischer, K. *J. Phys. Chem. B* **2000**, *104*, 6081.
- (23) Li, Y. J.; Oslonovitch, J.; Mazouz, N.; Plenge, F.; Krischer, K.; Ertl, G. *Science* **2001**, *291*, 2395.
- (24) Bonnefont, A.; Varela, H.; Krischer, K. *ChemPhysChem* **2003**, *4*, 1260.
- (25) Grauel, P.; Christoph, J.; Flätgen, G.; Krischer, K. *J. Phys. Chem. B* **1998**, *102*, 10264.
- (26) Krischer, K.; Varela, H.; Birzu, A.; Plenge, F.; Bonnefont, A. *Electrochim. Acta* **2003**, *49*, 103.
- (27) Strasser, P.; Eiswirth, M.; Ertl, G. *J. Chem. Phys.* **1997**, *107*, 991.
- (28) Conway, B. E.; Barnett, B.; Angerstein-Kozłowska, H.; Tilak, B. V. *J. Chem. Phys.* **1990**, *93*, 8361.
- (29) Flätgen, G.; Krischer, K. *J. Chem. Phys.* **1995**, *103*, 5428.
- (30) Bonnefont, A.; Varela, H.; Krischer, K. Unpublished results.
- (31) When CO is adsorbed at a potential close to the reversible hydrogen potential, a CO oxidation peak is observed at lower potentials in addition to the main CO oxidation peak. This peak is called a “pre-peak”. In contrast, when CO is adsorbed onto a Pt electrode in acidic media at a potential within the “double layer region”, a single CO oxidation peak is observed in the voltammogram.
- (32) Kita, H.; Shimazu, K.; Kunamitsu, K. *J. Electroanal. Chem.* **1988**, *241*, 163.
- (33) (a) Wieckowski, A.; Rubel, M.; Gutiérrez, C. *J. Electroanal. Chem.* **1995**, *382*, 97. (b) Couto, A.; Pérez, M. C.; Rincon, A.; Gutiérrez, C. *J. Phys. Chem.* **1996**, *100*, 19538.
- (34) Markovic, N. M.; Schmidt, T. J.; Grgur, B. N.; Gasteiger, H. A.; Behm, R. J.; Ross, P. N. *J. Phys. Chem. B* **1999**, *103*, 8568.
- (35) Markovic, N. M.; Lucas, C. A.; Rodes, A.; Stamenkovi, V.; Ross, P. N. *Surf. Sci.* **2002**, *499*, L149.